

Photodetachment anisotropy for mixed s - p states: $8/3$ and other fractions

Andrei Sanov,^{a)} Emily R. Grumbling,^{b)} Daniel J. Goebbert,^{c)} and Lori M. Culberson
Department of Chemistry and Biochemistry, The University of Arizona, Tucson, Arizona 85721, USA

(Received 16 August 2012; accepted 16 January 2013; published online 7 February 2013)

An approximate model for analytical prediction of photoelectron angular distributions in anion photodetachment from mixed s - p states is presented. Considering the dipole-allowed s , p , and d free-electron partial waves, the model describes photodetachment anisotropy in terms of the fractional p character of the initial orbital and the A and B coefficients describing the relative intensities of the $p \rightarrow d$ to $p \rightarrow s$ and $s \rightarrow p$ to $p \rightarrow s$ channels, respectively. The model represents an extension of the central-potential model to an intermediate regime encompassing varying degrees of s and p contributions to the initial bound orbital. This description is applicable to a broad class of hybrid molecular orbitals, particularly those localized predominantly on a single atom. Under the additional assumption of hydrogenic or Slater-type orbitals, the B/A ratio in photodetachment from a mixed $2s$ - $2p$ state is shown to equal $8/3$. Corresponding fractions are derived for other ns - np mixing cases. The predictions of the model are tested on several anion systems, including NH_2^- and CCl_2^- . The quantitative discrepancies in the latter case are attributed to the breakdown of the central-atom approximation and a mechanism for corresponding corrections is indicated. © 2013 American Institute of Physics. [<http://dx.doi.org/10.1063/1.4789811>]

I. INTRODUCTION

The photoelectron angular distributions (PADs) resulting from one-photon detachment or ionization provide insight into the properties of the parent orbitals.¹⁻⁴ If the initial state of the electron is described by a definite value of the orbital angular momentum quantum number, ℓ , as in the case of

atomic species, the emitted electrons are represented by superpositions of the dipole-allowed partial waves with $\ell_f = \ell \pm 1$. According to the derivations by Bethe⁵ generalized by Cooper and Zare,^{6,7} the anisotropy parameter^{1,6,7} β for photoemission using linearly polarized light in this case is given by the Cooper-Zare equation:

$$\beta = \frac{\ell(\ell-1)\chi_{\ell,\ell-1}^2 + (\ell+1)(\ell+2)\chi_{\ell,\ell+1}^2 - 6\ell(\ell+1)\chi_{\ell,\ell+1}\chi_{\ell,\ell-1}\cos(\delta_{\ell+1} - \delta_{\ell-1})}{(2\ell+1)[\ell\chi_{\ell,\ell-1}^2 + (\ell+1)\chi_{\ell,\ell+1}^2]}, \quad (1)$$

where $\chi_{\ell,\ell \pm 1}$ are the radial dipole matrix elements for the $\ell_f = \ell \pm 1$ partial waves, while $(\delta_{\ell+1} - \delta_{\ell-1})$ is the phase shift induced by interactions with the remaining neutral or cation.

Equation (1) is not generally applicable to molecular anions or any species, for which ℓ is not a good quantum number. In some cases, when the molecular orbital (MO) resembles an atomic-like wavefunction, an effective- ℓ description may be adopted. For example, the $2p\pi_g^*$ highest-occupied MO (HOMO) of O_2^- is a d -like function and the photodetachment of O_2^- can be modeled approximately using the central-

potential model^{6,7} with $\ell = 2$.⁸⁻¹⁰ However, most MOs cannot be assigned effective ℓ values, as any adequate description of their angular dependence must include multiple spherical harmonics with different values of ℓ .

Modeling the PADs in such cases is not a trivial pursuit, but direct computations that account for the complexity of the electronic structure, wave interference, relaxation effects, and orientation averaging have been successfully demonstrated.^{3,11-14} The rich mathematical details of such calculations may complicate the underlying physics of photoemission, in contrast to the transparent meaning of the Cooper-Zare equation. Hence, one often finds that intuitive physical insights require some simplifying assumptions. The objective of the present work is to tackle certain common cases of molecular anion photodetachment at a conceptual level, focusing not so much on the computational details, but on the formal analytical description of the process. The goal is, in essence, to describe the physics of photodetachment

^{a)} Author to whom correspondence should be addressed. Electronic mail: sanov@u.arizona.edu.

^{b)} AAAS Science and Technology Policy Fellow placed at the National Science Foundation (2012-2013). Any opinions, findings, and conclusions or recommendations expressed in this material are those of the author and do not necessarily reflect the views of the National Science Foundation.

^{c)} Present address: Department of Chemistry, The University of Alabama, Tuscaloosa, Alabama 35487, USA.

from several model molecular systems by relying, as much as possible, on a pen and paper only.

Specifically, we address the photodetachment from mixed s - p (hybrid sp^n) orbitals. Such orbitals are ubiquitous in chemistry, yet until recently¹⁵ there had been no analogue of the Cooper-Zare equation to describe the PADs in photodetachment from such mixed states. Intuitively, one expects the photodetachment from a mixed s - p state to fall into an intermediate realm between the pure s and pure p cases. We aim to provide an approximate analytical description of this intermediate regime.

As a starting point, we recently introduced an s - p mixing approach that describes the initial state as a linear combination of bound s and p orbitals.¹⁵ This approach is distinct from the so-called $s&p$ model,^{4,16} which considers the contributions of $s&p$ partial waves of the emitted (rather than bound) electrons. Here, we continue the development of the s - p mixing theory in the central-atom approximation (where the mixed s and p functions are localized on the same center) and apply the results to two model anions, NH_2^- and CCl_2^- . These anions and the specific transitions within them are chosen strategically to represent the following contrasting cases. First, the s - p mixed (HOMO-1) of NH_2^- is of predominantly p character, while the corresponding orbital in CCl_2^- has a large s component. Second, the NH_2^- initial state is well described within the central-atom approximation, while that of CCl_2^- is not.

In Sec. II, we introduce these model anions at summarize the experimental findings that will be used for evaluating the quality of the model. Section III is the heart of this work, where we develop a formal analytical description of the model and its parameters. Consistent with the above objectives, all derivations and calculations in Sec. III can be (have been) carried out in the most general form, using a pen and paper only. Section IV is devoted to the evaluation of the model parameters. Most analysis in this section is done by referencing the theory to relevant experimental results, still emphasizing formal analytical derivations rather than numerical calculations. Only in Sec. IV C do we involve electronic-structure calculations using the GAUSSIAN 98 software package.¹⁷ Throughout Secs. I–IV, we emphasize the generality of the model, while finally in Sec. V the model predictions are compared to the experimental results for the chosen anions. In light of the comparison, we re-evaluate the central-atom approximation and suggest remedies for dealing with the discrepancies.

II. MODEL ANIONS

Figure 1 gives a crude view of the NH_2^- and CCl_2^- electronic structures in the central-atom approximation. In each case, the b_1 symmetry HOMO has the dominant character of a non-bonding $2p(\pi)$ orbital of the central atom (nitrogen or carbon, respectively). The detachment of the b_1 HOMO electron yields the 2B_1 ground electronic state of neutral amidogen or the 1A_1 ground state of dichlorocarbene.¹⁸ Both a_1 (HOMO-1) orbitals are nominally non-bonding, hybrid lone-pair orbitals on the central atom. This description is a stag-

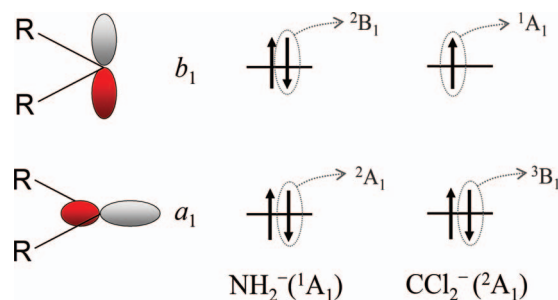


FIG. 1. Schematic illustration of the b_1 HOMO and a_1 (HOMO-1) orbitals of NH_2^- and CCl_2^- (in the central-atom approximation—see the text for details). The b_1 HOMO has the dominant character of a non-bonding $2p$ orbital of N or C, respectively. The detachment of the b_1 electron yields the 2B_1 ground electronic state of NH_2 or the 1A_1 ground state of CCl_2 . The a_1 (HOMO-1) orbital in each case is a nominally sp^n hybrid (lone-pair) orbital, regarded as predominantly a non-bonding $2p(\sigma)$ orbital on the central atom. Detachment of the (β spin) a_1 electron accesses the 2A_1 excited state of NH_2 or the 3B_1 state of CCl_2 .

gering oversimplification, particularly for CCl_2^- , as discussed later in this paper. Detachment of the β -spin a_1 electron from the anion accesses the 2A_1 excited state of NH_2 or the 3B_1 state of CCl_2 , respectively.

The relevant experimental results for these species are presented in Figure 2 (NH_2^-) and Figure 3 (CCl_2^-). Details of the photoelectron imaging experiments are given in the Appendix and Refs. 4 and 19–21. Both anions have also been studied using photoelectron spectroscopy by other groups.^{18,22–25} As our findings are consistent with the past results, we shall limit the discussion to the data in Figures 2 and 3 only. The photoelectron spectra in Figs. 2(a) and 3(a) reveal two bands each, corresponding to detachment from the b_1 (pure p) HOMO and a_1 (mixed s - p) HOMO-1 orbitals of NH_2^- and CCl_2^- , respectively. The NH_2^- image and spectrum in Figure 2(a) were reported previously as part of the $\text{NH}_2^-(\text{NH}_3)_n$ dataset, in our work concerned exclusively with the 2B_1 transition.¹⁹ The present work will focus on the a_1^{-1} transitions, i.e., the 2A_1 band in Figure 2(a) and the 3B_1 band in Figure 3(a), as the corresponding initial orbitals may be described approximately as hybrids of the $2s$ and $2p$ atomic orbitals of the central atom.

The qualitatively different characters of the a_1 HOMO and b_1 (HOMO-1) orbitals in these anions are immediately apparent in the photoelectron angular distributions—see, for example, the different PADs of the two bands in the CCl_2^- photoelectron image in Figure 3(a). There, the PAD of the b_1^{-1} channel, yielding 1A_1 neutral carbene, is perpendicular ($\beta < 0$), characteristic of moderate-energy photodetachment from a p -like state (as, for example, in O^- and I^- photodetachment^{26–31}). On the other hand, the a_1^{-1} PAD, corresponding to the 3B_1 neutral state, is sharply parallel ($\beta > 0$), approaching the Cooper-Zare model prediction for pure s state photodetachment. Thus, the PADs suggest that the a_1 (HOMO-1) of CCl_2^- is in fact of predominantly s character, contrary to the nominal sp^2 hybridization picture.

The quantitative anisotropy data for the respective NH_2^- and CCl_2^- a_1^{-1} detachment transitions, are plotted (as

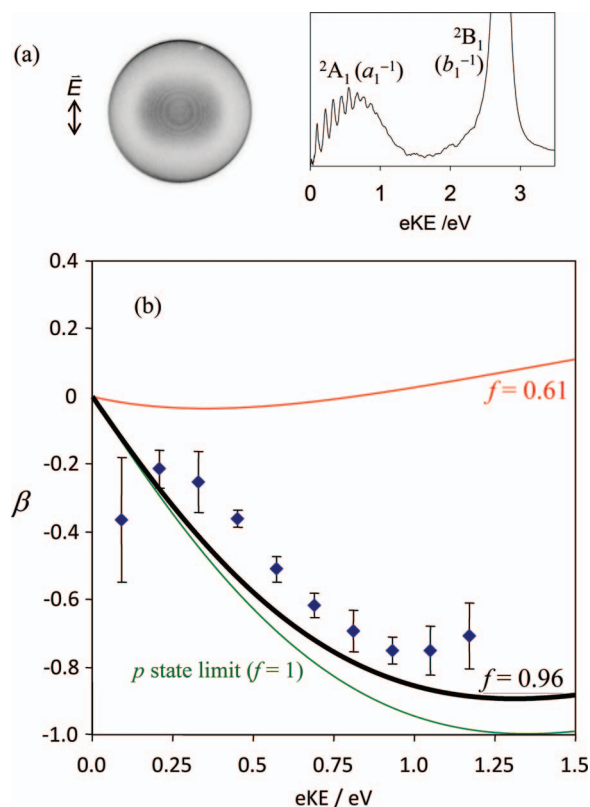


FIG. 2. Photoelectron imaging results for NH_2^- . (a) 355 nm photoelectron image (arbitrary velocity and intensity scales) and the corresponding photoelectron spectrum. (b) Symbols: the anisotropy data for the ${}^2A_1(a_1^{-1})$ band. Green curve: the WBCZ model prediction for pure p state photodetachment, calculated using Eq. (6) with $f = 1$, Eq. (7) with $Z = 0$ or, equivalently, Eq. (2) with $\ell = 1$. Red curve: s - p mixing curve calculated using the unmodified result of Eq. (32), $B/A = 8/3$, and assuming the fractional p character of the parent a_1 orbital $f = 0.61$ ($Z = 1.7$), from the uncorrected *ab initio* central-atom prediction. Bold black curve: model prediction using $f = 0.96$, corrected for the contributions of the H atom orbitals ($Z = 0.11$). All model calculations assume $A = 0.37 \text{ eV}^{-1}$ and $\cos(\delta_2 - \delta_0) = 1$.

symbols) versus electron kinetic energy ($\text{eKE} \equiv \varepsilon$) in Figures 2(b) and 3(b). The PADs are indeed intermediate between the pure s and pure p state limits, with CCl_2^- data falling closer to s and NH_2^- to p . The remainder of this paper develops a model description of these trends.

III. THE MODEL

A. Model approximations and formalism

1. Hanstorp's approximation

The Cooper-Zare equation (Eq. (1)) can be rearranged to show that β is dependent not on the matrix elements themselves, but the ratio of $\chi_{\ell, \ell+1}$ to $\chi_{\ell, \ell-1}$. In anion photodetachment, in particular, this ratio is often assumed to vary linearly with electron kinetic energy. This simplification, originally noted by Hanstorp *et al.*,²⁶ follows from the Wigner law³² for near-threshold photodetachment, $\sigma_{\ell_f} \propto \varepsilon^{\ell_f+1/2}$, as the partial cross-sections are proportional to the

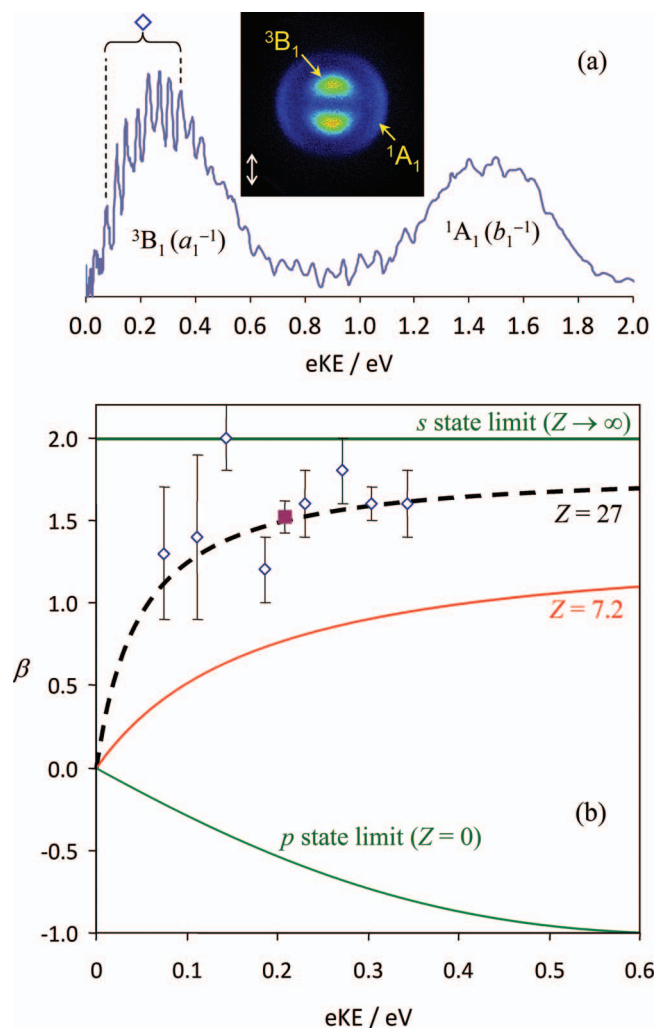


FIG. 3. Photoelectron imaging results for CCl_2^- . (a) 355 nm photoelectron image (arbitrary velocity and intensity scales) and the corresponding photoelectron spectrum. (b) Symbols: photoelectron anisotropy data for the partially resolved vibrational peaks of the ${}^3B_1(a_1^{-1})$ band, indicated with the same diamond symbol in (a). The purple square corresponds to the overall anisotropy parameter calculated by integration over the entire 3B_1 band. Green curves: the WBCZ model predictions for pure s and pure p state photodetachment, calculated using Eq. (6) with $f = 0$ or 1, Eq. (7) with $Z \rightarrow \infty$ or $Z = 0$, as indicated, or, equivalently, using Eq. (2) with $\ell = 0$ or 1, respectively. Red curve: the s - p mixing curve calculated using $B/A = 8/3$ (Eq. (32)) and assuming the fractional p character of the parent a_1 orbital $f = 0.27$, from the uncorrected *ab initio* central-atom prediction ($Z = 7.2$). Dashed black curve: the only simulation in this work involving a fit of the s - p mixing equation (Eq. (7)) to experimental data. It corresponds to $Z = 27$, which can be obtained, for example, by assuming $f = 0.27$ and $B/A = 10$ or $f = 0.09$ and $B/A = 8/3$, as discussed in Sec. V B. All model calculations for CCl_2^- assume $A = 0.75 \text{ eV}^{-1}$ and $\cos(\delta_2 - \delta_0) = 1$.

squares of the corresponding matrix elements, $\sigma_{\ell_f} \propto \chi_{\ell, \ell_f}^2$ ($\ell_f = \ell \pm 1$).

Assuming $\sigma_{\ell+1}/\sigma_{\ell-1} \propto \varepsilon^2$ and, therefore, $\chi_{\ell, \ell+1}/\chi_{\ell, \ell-1} = A_\ell \varepsilon$, where A_ℓ is a proportionality coefficient, Eq. (1) can be rearranged to allow the calculation of β as an explicit function of ε , via the formula that we shall refer to as the Wigner–Bethe–Cooper–Zare (WBCZ) equation:²⁶

$$\beta(\varepsilon) = \frac{\ell(\ell-1) + (\ell+1)(\ell+2)A_\ell^2\varepsilon^2 - 6\ell(\ell+1)A_\ell\varepsilon \cos(\delta_{\ell+1} - \delta_{\ell-1})}{(2\ell+1)[\ell + (\ell+1)A_\ell^2\varepsilon^2]}. \quad (2)$$

2. One-electron, single-center, and s - p mixing approximations

As in the previous work,¹⁵ we consider single-photon, one-electron photodetachment from a state represented as a linear combination of one s and one p type function localized on the same center (“central atom”) in the molecular frame:

$$|\psi_i\rangle = \sqrt{1-f}|s\rangle + \sqrt{f}|p\rangle, \quad (3)$$

with f being the fractional p character of the state, $0 \leq f \leq 1$. Any relative phase factors for the s and p contributions are absorbed into the corresponding kets. In our previous work,¹⁵ Eq. (3) was used to describe an s -like state polarized by solvation interactions, but due to the non-perturbative nature of the model, it can also be applied to a broad class of mixed (hybrid) s - p orbitals. In this work, Eq. (3) will be used to approximate canonical Hartree-Fock orbitals. However, without much extra effort or loss of generality the same approach can be applied to Dyson orbitals that include correlation and relaxation effects.^{13,14,33}

Photodetachment from a one-electron mixed state described by Eq. (3) will generally yield s , p , and d electric-dipole allowed partial waves via the $s \rightarrow p$ and $p \rightarrow s$, d transitions. The resulting PAD will reflect the eKE-dependent relative contributions of these waves. Assuming, as before,²⁶ the Wigner-law³² scaling of the partial cross-sections, we may write

$$\frac{\sigma_2}{\sigma_0} = \frac{\chi_{1,2}^2}{\chi_{1,0}^2} = A^2\varepsilon^2, \quad (4)$$

$$\frac{\sigma_1}{\sigma_0} = \frac{\chi_{0,1}^2}{\chi_{1,0}^2} = B\varepsilon, \quad (5)$$

where A and B are constant model parameters, while $\chi_{\ell, \ell \pm 1}$ are the radial dipole integrals for the corresponding $\ell \rightarrow \ell \pm 1$ transitions.

Parameter A in Eq. (4) is a specific case ($\ell = 1$) of the familiar A_ℓ coefficient appearing in Eq. (2). It describes the relative scaling of the $p \rightarrow s$ and $p \rightarrow d$ channels. Throughout this work, we adopt the notation $A \equiv A_1$, i.e., no-subscript A describes the detachment from a p state or a p component of a mixed state. Other types of detachment processes will also be considered, in particular the $d \rightarrow p$ and $d \rightarrow f$ transitions, for which the A_ℓ coefficient will always be explicitly denoted A_2 (i.e., $\chi_{2,3}/\chi_{2,1} = A_2\varepsilon$, per Eq. (4)).

Parameter B in Eq. (5) was originally introduced in the previous work¹⁵ in order to describe, in a similar way, the relative scaling of the $s \rightarrow p$ and $p \rightarrow s$ channels. No generalizations of the B coefficient for other types of mixed states have been developed in the literature.

Under the assumptions of Eqs. (3)–(5), the anisotropy parameter β can be expressed as an explicit function of eKE:¹⁵

$$\beta = \frac{2(1-f)B\varepsilon + 2fA^2\varepsilon^2 - 4fA\varepsilon \cos(\delta_2 - \delta_0)}{f + 2fA^2\varepsilon^2 + (1-f)B\varepsilon}. \quad (6)$$

This result differs from the WBCZ model (Eq. (2)) in that it describes photodetachment from a mixed s - p orbital, rather than a state with a defined ℓ value. In the limiting cases $f = 0$ and $f = 1$, Eq. (6) reduces exactly to the respective WBCZ predictions for detachment from pure s and pure p states. For mixed states ($f \neq 0$), we rearrange Eq. (6) as follows:

$$\begin{aligned} \beta &= \frac{2\frac{1-f}{f}\frac{B}{A}\varepsilon + 2A\varepsilon^2 - 4\varepsilon \cos(\delta_2 - \delta_0)}{\frac{1}{A} + 2A\varepsilon^2 + \frac{1-f}{f}\frac{B}{A}\varepsilon} \\ &= \frac{2Z\varepsilon + 2A\varepsilon^2 - 4\varepsilon \cos(\delta_2 - \delta_0)}{1/A + 2A\varepsilon^2 + Z\varepsilon}. \end{aligned} \quad (7)$$

Thus, aside from the phase shift, the model anisotropy trends $\beta(\varepsilon)$ are determined by only two parameters, A and $\frac{1-f}{f}\frac{B}{A} \equiv Z$, rather than three (A , B , and f), as may appear at first from Eq. (6). The meaning of the newly introduced parameter Z is transparent: for a given A , it describes the relative intensities of the $s \rightarrow p$ and $p \rightarrow s$ channels (via B), weighted by the relative contributions of the s and p components to the initial state, $(1-f)/f$. The asymptotic value of Z for a pure s state is $Z \rightarrow \infty$, while that for a p state is $Z = 0$.

As in the previous work,^{15,19} we will neglect the phase shift in Eqs. (6) and (7) by setting $\cos(\delta_2 - \delta_0) = 1$. The appropriate values of A for each case will be determined from experimental data, while Z (or, equivalently, B/A and f) will be found from *ab initio* analysis. The model predictions will be compared to the experimental results.

B. Free-electron waves

We now turn to explicit evaluation of the A and B coefficients in Eqs. (6) and (7). The radial dipole integrals defining A and B via Eqs. (4) and (5) are $\chi_{\ell, \ell \pm 1} \equiv \langle R_{free, \ell \pm 1} | r | R_{n, \ell} \rangle$, assuming that the bound orbitals and the free-electron waves are defined as the respective radial functions, $R_{n, \ell}$ and $R_{free, \ell \pm 1}$, multiplied by the corresponding spherical harmonics. Assuming no interaction of the continuum electron with the remaining neutral, the photodetached electron can be represented by free spherical waves. The radial functions $R_{free, \ell}(r)$ are then proportional to spherical Bessel functions $j_\ell(kr)$.^{34,35} In particular, the s , p , and d partial waves are represented, respectively, by

$$j_0(kr) = \frac{\sin kr}{kr}, \quad (8)$$

$$j_1(kr) = \frac{\sin kr}{(kr)^2} - \frac{\cos kr}{kr}, \quad (9)$$

$$j_2(kr) = \left(\frac{3}{(kr)^2} - 1 \right) \frac{\sin kr}{kr} - \frac{3 \cos kr}{(kr)^2}. \quad (10)$$

The proportionality coefficients between $j_\ell(kr)$ and $R_{free, \ell}(r)$ depend on the normalization condition applied to the free-electron waves. Two common normalization scales are discussed in Supplement A of the supplementary material.³⁶

For the so-called $k/2\pi$ scale, $R_{free, \ell}(r)$ are normalized per $k/2\pi$ interval, where k is the wavenumber corresponding to electron momentum, $k = p/h$. The corresponding normalized radial functions, denoted explicitly $R_{k, \ell}(r)$, have the form,³⁴

$$R_{k, \ell}(r) = 2kj_\ell(kr). \quad (11)$$

Another textbook variant of momentum-space normalization is the k (rather than $k/2\pi$) scale, whereas the radial functions trivially differ from those in Eq. (11) by a factor of $\sqrt{2\pi}$.³⁵

Since comparisons to the experiment are usually done in the energy domain, it is convenient (but not strictly necessary) to employ the alternative ε scale normalization per energy interval.³⁷ This normalization was adopted, for example, in the works of Bethe³⁸ and Goldberg *et al.*³⁹ The ε scale normalized functions, denoted $R_{\varepsilon, \ell}(r)$ and expressed in atomic units, have the form,

$$R_{\varepsilon, \ell}(r) = \sqrt{\frac{2k}{\pi}} j_\ell(kr). \quad (12)$$

The results of this work are not affected by the choice of normalization. Nonetheless, the normalization coefficients in Eqs. (11) and (12) do include photoelectron momentum, k . For this reason, care should be taken in transformations between the $k/2\pi$ and ε spaces, in order to preserve the proper scaling of partial photodetachment cross-sections (see Supplement A of the supplementary material).³⁶

C. Radial dipole integrals and the A , B coefficients

The radial dipole integrals $\chi_{\ell, \ell \pm 1} \equiv \langle R_{free, \ell \pm 1} | r | R_{n, \ell} \rangle$ are defined by one of the following explicit expressions, depending on the type of normalization employed. In momentum space,

$$\chi_{\ell, \ell \pm 1}^k = \int_0^\infty R_{k, \ell \pm 1}(r) r R_{n, \ell}(r) r^2 dr, \quad (13)$$

while in energy space,³⁹

$$\chi_{\ell, \ell \pm 1}^\varepsilon = \int_0^\infty R_{\varepsilon, \ell \pm 1}(r) r R_{n, \ell}(r) r^2 dr, \quad (14)$$

where the superscript k and ε indicate the corresponding normalization scale ($k/2\pi$ or ε , respectively). The additional r^2 terms under the integrals arise from three-dimensional infinitesimal volume in spherical polar coordinates.

Substituting either Eq. (11) into Eq. (13) or, equivalently, Eq. (12) into Eq. (14) and using the result in Eqs. (4) and (5), the following explicit definitions of the A and B coefficients are obtained:

$$A_\varepsilon = \frac{\chi_{1,2}}{\chi_{1,0}} = \frac{\int_0^\infty j_2(kr) r^3 R_{np}(r) dr}{\int_0^\infty j_0(kr) r^3 R_{np}(r) dr}, \quad (15)$$

$$B_\varepsilon = \frac{\chi_{0,1}^2}{\chi_{1,0}^2} = \frac{\left(\int_0^\infty j_1(kr) r^3 R_{n's}(r) dr \right)^2}{\left(\int_0^\infty j_0(kr) r^3 R_{np}(r) dr \right)^2}, \quad (16)$$

where $R_{ns}(r) \equiv R_{n,0}(r)$ and $R_{np}(r) \equiv R_{n,1}(r)$ represent the s and p components of the initial (bound) orbital. The prime in $R_{n's}(r)$ in Eqs. (16) indicates that the s and p components of the initial state do not have to correspond to the same principal quantum number. (For example, solvation-induced polarization of H^- was described by a small $2p$ -type contribution added to the $1s$ orbital, i.e., $n' = 1$ and $n = 2$.^{15,19}) In Eqs. (15) and (16), the k or ε indexes for $\chi_{\ell, \ell \pm 1}$ have been omitted, as the normalization coefficients for $R_{k, \ell}(r)$ or $R_{\varepsilon, \ell}(r)$ cancel out in both cases and hence the type of normalization used does not affect the radial element ratios. (However, the individual scaling of the radial elements does depend on wavefunction normalization, as discussed in Supplement A of the supplementary material.)³⁶

From Eqs. (15) and (16), the B/A ratio can be calculated as

$$\frac{B}{A} = \frac{\left(\int_0^\infty j_1(kr) r^3 R_{n's}(r) dr \right)^2}{\int_0^\infty j_0(kr) r^3 R_{np}(r) dr \int_0^\infty j_2(kr) r^3 R_{np}(r) dr}. \quad (17)$$

Similar to the $\chi_{\ell, \ell \pm 1}$ ratios and the individual A and B coefficients in Eqs. (15) and (16), B/A defined by Eq. (17) is independent of the type of normalization chosen for the free-electron radial functions. However, since the integrals in Eqs. (15)–(17) depend parametrically on k (and, therefore, ε), so do, in general, the A and B coefficients and the B/A ratio. This dependence vanishes only in the Wigner-like low-eKE limit, as discussed in Sec. III E.

Equation (15) defines the A coefficient for detachment from either a pure p orbital, or from the p component of a mixed orbital (i.e., $A \equiv A_1$ in the more general notation of Eq. (2)). The equation is easily generalized for photodetachment from any $n\ell$ ($n > \ell \geq 1$) orbital, as follows:

$$A_{\ell\varepsilon} = \frac{\chi_{\ell, \ell+1}}{\chi_{\ell, \ell-1}} = \frac{\int_0^\infty j_{\ell+1}(kr) r^3 R_{n, \ell}(r) dr}{\int_0^\infty j_{\ell-1}(kr) r^3 R_{n, \ell}(r) dr}. \quad (18)$$

Equation (16) for the B coefficient, on the other hand, cannot be generalized in a similar fashion, because Eq. (6), where this coefficient first appears, was derived for the specific case of photodetachment from a mixed s - p orbital.

D. Low-eKE approximation

We now turn to the Wigner-like slow-electron limit,^{32,40,41} originally assumed by Hanstorp *et al.*²⁶ to define the A_ℓ constant in Eq. (2). This limit is defined by $kr \ll 1$ in the region of significant overlap of the free-electron waves and the initial bound state. If the extent of the initial state is assumed to be on the order of the Bohr radius a , the above condition corresponds to $ka \ll 1$ or $\varepsilon \ll \hbar^2/2ma^2 = 1/2$ a.u. = 13.6 eV. However, this estimate is misleading, as non-trivial magnitudes of most anionic orbitals of interest extend to multiples of a , so the low-eKE condition is in fact far more restrictive, expressed rather as $\varepsilon \ll 1$ eV. The role of very diffuse asymptotic tails of anion orbitals in photodetachment processes is well known¹⁴ and further

emphasized throughout this article and in Supplement B of the supplementary material.³⁶

The slow-electron approximation implied in Eq. (2) is, nonetheless, commonly and successfully used to interpret PADs in anion photodetachment over broad ranges of eKE (up to several eV). In what follows, we too adopt this approximation, as our objective is to generalize the WBCZ equation (Eq. (2)) to the mixed s - p case (Eq. (6)); in order to do so, one must rely on similar fundamental assumptions. The robustness and the limitations of this approach, specifically, why it seems to work even outside the strict Wigner-like regime, are touched upon in Supplement C of the supplementary material.³⁶

In the Wigner limit ($kr \rightarrow 0$), the spherical Bessel functions can be replaced by the leading terms of their Maclaurin series expansions, giving rise to the known origin behavior,^{34,35}

$$j_\ell(kr) \cong \frac{(kr)^\ell}{(2\ell + 1)!!}, \quad \text{for } kr \rightarrow 0. \quad (19)$$

The specific $\ell = 0 - 2$ functions in Eqs. (8)–(10) behave as $j_0(kr) \cong 1$, $j_1(kr) \cong kr/3$, $j_2(kr) \cong (kr)^2/15$.

Substituting the above origin terms for j_0 and j_2 into Eq. (15) yields the following expression for the A coefficient for detachment from a pure p or a mixed s - p orbital:

$$A\varepsilon = \frac{k^2 \int_0^\infty r^5 R_{np}(r) dr}{\int_0^\infty r^3 R_{np}(r) dr}, \quad (20)$$

or, since $\varepsilon = k^2/2$ (atomic units),

$$A = \frac{2 \int_0^\infty r^5 R_{np}(r) dr}{15 \int_0^\infty r^3 R_{np}(r) dr}. \quad (21)$$

Similarly, substituting $j_0(kr) \cong 1$ and $j_1(kr) \cong kr/3$ into Eq. (16), we obtain an explicit expression for B for detachment from a mixed s - p orbital,

$$B\varepsilon = \frac{\left(\frac{k}{3} \int_0^\infty r^4 R_{n's}(r) dr\right)^2}{\left(\int_0^\infty r^3 R_{np}(r) dr\right)^2} \quad (22)$$

or, using $\varepsilon = k^2/2$,

$$B = \frac{2 \left(\int_0^\infty r^4 R_{n's}(r) dr\right)^2}{9 \left(\int_0^\infty r^3 R_{np}(r) dr\right)^2}. \quad (23)$$

From Eq. (17) or, equivalently, Eqs. (21) and (23), the B/A ratio is calculated as

$$\begin{aligned} \frac{B}{A} &= \frac{\left(\frac{k}{3} \int_0^\infty r^4 R_{n's}(r) dr\right)^2}{\left(\int_0^\infty r^3 R_{np}(r) dr\right) \left(\frac{k^2}{15} \int_0^\infty r^5 R_{np}(r) dr\right)} \\ &= \frac{5 \left(\int_0^\infty r^4 R_{n's}(r) dr\right)^2}{3 \int_0^\infty r^3 R_{np}(r) dr \int_0^\infty r^5 R_{np}(r) dr}. \end{aligned} \quad (24)$$

Despite the explicit energy dependence of the integrals in Eqs. (15)–(17), parameters A and B , as well as the B/A ratio, are indeed independent of k and, therefore, ε in the slow-electron limit, as evident from Eqs. (21), (23), and (24). These conclusions are consistent with the Wigner law³² and the formulations by Hanstorp *et al.*²⁶

E. Photodetachment from hydrogenic s - p orbitals

If the s and p components of the detachment orbital are assumed to be hydrogenic, with the principal quantum number n and effective nuclear charge ξ_{ns} and ξ_{np} , respectively, all integrals in Eqs. (21), (23), and (24) can be evaluated analytically using a pen and paper only. Their values for up to $n = 6$ are summarized in Table S.4 in Supplement D of the supplementary material.³⁶ Substituting these results in Eqs. (21), (23), and (24) gives the A and B coefficients and/or the B/A ratio within the model approximations.

We illustrate these calculations on the $2s$ - $2p$ case, which applies to the a_1 (HOMO–1) orbitals of NH_2^- and CCl_2^- . Using the hydrogenic $2s$ and $2p$ radial functions (Table S.3 of the supplementary material)³⁶

$$R_{2s}(r) = \frac{1}{\sqrt{2}} \xi_{2s}^{3/2} (1 - \xi_{2s} r/2) e^{-\xi_{2s} r/2}, \quad (25)$$

$$R_{2p}(r) = \frac{1}{2\sqrt{6}} \xi_{2p}^{5/2} r e^{-\xi_{2p} r/2}, \quad (26)$$

the integrals in Eqs. (21), (23), and (24) are evaluated as (Table S.4 of the supplementary material).³⁶

$$\int_0^\infty r^4 R_{2s}(r) dr = -\frac{4! \cdot 2^7}{\sqrt{2} \xi_{2s}^{7/2}}, \quad (27)$$

$$\int_0^\infty r^3 R_{2p}(r) dr = \frac{4! \cdot 2^4}{\sqrt{6} \xi_{2p}^{5/2}}, \quad (28)$$

$$\int_0^\infty r^5 R_{2p}(r) dr = \frac{6! \cdot 2^6}{\sqrt{6} \xi_{2p}^{9/2}}. \quad (29)$$

Substituting Eqs. (27)–(29) into Eqs. (21) and (24) gives

$$A = \frac{2}{15} \frac{6! \cdot 2^6}{\sqrt{6} \xi_{2p}^{9/2}} \frac{\sqrt{6} \xi_{2p}^{5/2}}{4! \cdot 2^4} = \frac{16}{\xi_{2p}^2} \text{Hartree}^{-1} \approx (0.588/\xi_{2p}^2) \text{eV}^{-1} \quad (30)$$

and

$$\frac{B}{A} = \frac{5}{3} \left(-\frac{4! \cdot 2^7}{\sqrt{2} \xi_{2s}^{7/2}} \right)^2 \frac{\sqrt{6} \xi_{2p}^{5/2}}{4! \cdot 2^4} \frac{\sqrt{6} \xi_{2p}^{9/2}}{6! \cdot 2^6} \quad (31)$$

$$\frac{B}{A} = \frac{8}{3} \left(\frac{\xi_{2p}}{\xi_{2s}} \right)^7.$$

Note the high-power dependence of B/A on ξ_{2p}/ξ_{2s} . If, however, the $2s$ and $2p$ effective nuclear charges are assumed equal, the result in Eq. (31) simplifies further to

$$\frac{B}{A} = \frac{8}{3}. \quad (32)$$

To reflect on the nature of the $\xi_{2p} = \xi_{2s}$ assumption, consider that the r^5 , r^4 , and r^3 terms under the integrals in Eqs. (21), (23), and (24) lend determining roles in the calculations of A , B , and B/A to the large- r parts of the corresponding anionic wavefunctions. The effective charge in this case should be viewed as a parameter describing the behavior of these very diffuse tails, rather than the divergent degrees of core penetration (commonly described with $\xi_{2s} \neq \xi_{2p}$). Both the $2s$ and $2p$ tails interact with a similarly charged, nearly

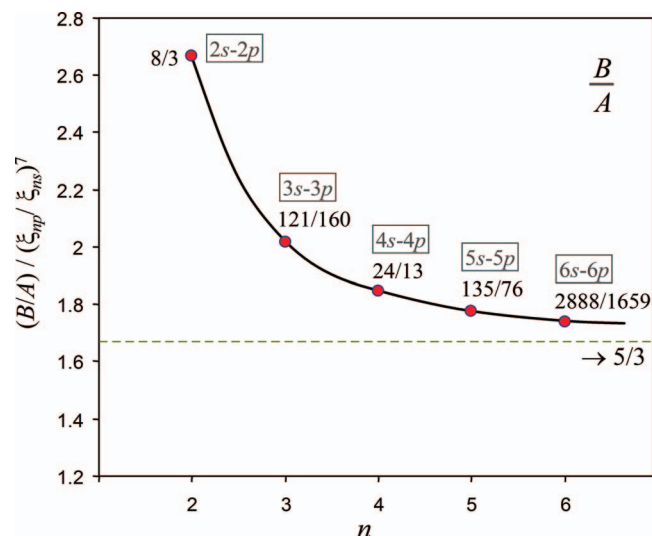


FIG. 4. The B/A ratios for different ns - np mixing cases ($n = 2$ – 6) calculated for hydrogenic orbitals by substituting the integrals from Table S.4 in Supplement D of the supplementary material³⁶ into Eq. (24). The continuous curve is intended as a guide. The fractions indicated next to the data points correspond to $\xi_{ns} = \xi_{np}$. For $\xi_{ns} \neq \xi_{np}$, the B/A ratios are equal to the indicated fractions multiplied by $(\xi_{np}/\xi_{ns})^7$.

neutral core and hence the assumption $\xi_{2p} = \xi_{2s}$ seems reasonable, to a degree.

Calculations for other ns - np mixing cases show that B/A varies gradually with n . Using the integrals from Table S.4 (Supplement D of the supplementary material)³⁶ in Eq. (24) and assuming $\xi_{ns} = \xi_{np}$, we obtain $B/A = 121/160$ for the $3s$ - $3p$ mixing, $B/A = 24/13$ for $4s$ - $4p$, $B/A = 135/76$ for $5s$ - $5p$, etc. These fractions are plotted as a function of n in Figure 4 and are easily generalized for mixed hydrogenic states with $\xi_{ns} \neq \xi_{np}$. It is apparent from Figure 4 that as n increases (e.g., for Rydberg-like dipole-bound states) B/A approaches the asymptotic limit of $5/3$.

Similar calculations can be carried out for the off-diagonal $n's$ - np states with $n' \neq n$. In one case, the perturbation of H^- by solvation was described by adding a small polarization component, mathematically described as a $2p$ type function, to the $1s$ orbital of the anion.^{15,19} Using Table S.4 of the supplementary material³⁶ and Eq. (24), we find that in the $1s$ - $2p$ scenario $B/A = (1/768)(\xi_{2p}/\xi_{1s})^7$. The assumption $\xi_{1s} = \xi_{2p}$ would not be appropriate, even approximately, in this case. In fact, $\xi_{1s} > \xi_{2p}$ is expected, due to the very diffuse nature of the solvation-induced polarization component.

IV. EVALUATION OF THE MODEL PARAMETERS

Given specific values of A and $Z \equiv (B/A)(1 - f)/f$, the $\beta(\epsilon)$ trends in photodetachment from mixed s - p orbitals can be modeled using Eqs. (6) or (7). This section discusses the numerical values of these parameters, while comparison to experimental data is presented in Sec. V.

The formalism developed in Sec. III describes molecular anion photodetachment as a transition from an orbital that belongs to one “central” atom only: N in NH_2^- and C in CCl_2^- . Thus, the A and B coefficients are essentially atomic proper-

ties. To illuminate the implications and limitations of the results so far, we focus first on the more familiar A coefficient.

A. The A coefficients for O^- and C^-

In modeling the photodetachment from NH_2^- and CCl_2^- within the central-atom approximation, it would be natural to first consider the detachment from the corresponding atomic anions. Since only limited data are available for C^- ,^{42,43} while N^- does not exist, we first undertake further model development on the example of O^- . Theoretical predictions for this anion can be compared to the known value of $A = 0.55 \pm 0.045 \text{ eV}^{-1}$, determined through empirical fitting of the WBCZ equation (Eq. (2)) to experimental data.^{26–28,42,44} We will then extend the discussion to C^- , while the A coefficient for the nitrogen center in NH_2^- will be determined in Sec. IV B by analyzing the results for N_3^- photodetachment.

1. O^- photodetachment

Equation (30) is consistent with the experimental result for O^- assuming $\xi_{2p} \approx 1$. To put this estimate in perspective, consider that the r^5 and r^3 terms under the integrals in Eq. (21) lend a determining role in calculations of A to the diffuse long-range tails of anionic wavefunctions. The tails interact with a nearly neutral core, asymptotically corresponding to $\xi_{2p} \rightarrow 0$. At the other extreme is the prediction derived from Slater’s rules,^{45,46} $\xi_{2p} = 4.2$. This estimate is also not appropriate for our analysis, as it does not describe the diffuse parts of the orbitals. The above value of $\xi_{2p} \approx 1$ is a compromise between the two extremes.

Additional insight into the role of diffuse functions can be gained from Eq. (21), which allows the calculation of A from any radial function $R_{np}(r)$. Using this equation, the effective-charge description of the bound $2p$ orbital (Eq. (26)) can be replaced with a function derived from *ab initio* calculations. This analysis, using O^- as a model system, is presented in Supplement B of the supplementary material,³⁶ where we demonstrate that such calculations, employing standard Gaussian basis sets, significantly underestimate the value of A . The error is traced to the inadequate description of the long-range tails of anion orbitals with Gaussian basis functions and can be remedied by complementing the description with diffuse Slater orbital functions.

2. C^- photodetachment

Photodetachment of many organic anions removes electrons from carbon-based orbitals. Hence, understanding C^- photodetachment is an important step in modeling these systems. The electron affinity of atomic carbon is well known (1.262 eV),⁴⁷ but only limited data exist for C^- PADs. The known data points are shown in Figure 5 and include measurements for the ground-state $\text{C}^-(^4\text{S})$ (filled symbols)^{42,43} and excited-state $\text{C}^-(^2\text{D})$ (open symbols).^{43,48} Although in all cases the electrons originate from $2p$ orbitals, the $\text{C}^-(^4\text{S})$ results are most relevant to this discussion. Modeling this limited dataset using Eq. (2) with no phase-shift (solid curve in

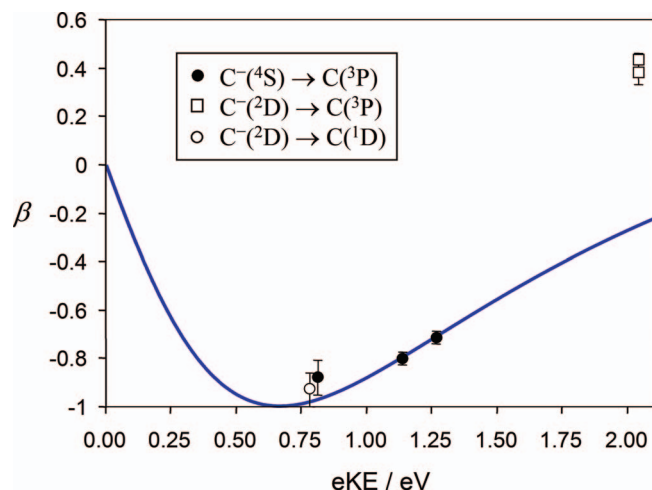


FIG. 5. Experimental photoelectron anisotropy parameter values in C^- photodetachment vs. eKE . Filled circles: $C^-(^4S) \rightarrow C(^3P)$ results from Refs. 42 and 43; squares: $C^-(^2D) \rightarrow C(^3P)$ data from Refs. 48 and 43; open circle: $C^-(^2D) \rightarrow C(^1D)$ value from Ref. 43. Solid curve: WBCZ model prediction (Eq. (2)) with $A = 0.75 \text{ eV}^{-1}$ and $\cos(\delta_2 - \delta_0) = 1$.

Figure 5) yields $A \approx 0.75 \text{ eV}^{-1}$. As pointed out by Hanstorp *et al.*²⁶ and evident from Eq. (21), A reflects the spatial extent of the anion wavefunction. Despite the scarcity of experimental data, the larger value of A for C^- (0.75 eV^{-1}), compared to that for O^- (0.55 eV^{-1}) is consistent with the relative “sizes” of these anions.

The above value $A = 0.75 \text{ eV}^{-1}$ is used for calculating all CCl_2^- model curves in Figure 3(b). It can be argued that this value should be modified to account for the greater binding energy of the a_1 orbital in CCl_2^- (VDE $\approx 3.2 \text{ eV}$ for the 3B_1 band in Figure 3(a)), compared to the $2p$ orbital of C^- [eBE = 1.262 eV for $C^-(^4S)$ relative to $C(^3P)$]. The reasoning behind such an adjustment is discussed in Sec. IV B on the O_2^- example. However, the greater binding energy of the carbene, compared to atomic carbon, can be attributed to the significant density of this orbital on the halogen atoms and thus falls under the limitations of the central-atom approximation. Hence, we use the unmodified value of A to model the CCl_2^- data, while the effect of the breakdown of the central-atom approximation is discussed in Sec. V B.

B. Extension to molecular anions

1. The O_2^- example

In some cases, the above formalism for calculating A or, more generally, A_ℓ can be extended to molecular anions. We illustrate the process by obtaining a model prediction for A_2 for O_2^- from the known experimental value of $A = 0.55 \text{ eV}^{-1}$ for O^- . The model prediction is then compared to the result of fitting the WBCZ equation (Eq. (2)) to a significant volume of O_2^- experimental data.^{9,10,49,50} Once the self-consistency of the model is confirmed, it may be applied to other cases.

Due to vibronic coupling, the experimental value of A_2 for O_2^- depends on the vibrational state of neutral O_2 , ranging from $0.43(2) \text{ eV}^{-1}$ for $v = 0$ to $0.31(5) \text{ eV}^{-1}$ for $v = 6$.¹⁰ As the vibronic effects are not part of the present work,

$A_2 = 0.40(1) \text{ eV}^{-1}$,¹⁰ corresponding to the (nearly) vertical detachment transition to $v = 2$,⁵¹ is perhaps most appropriate for model comparisons.

In the approximate central-potential description of O_2^- photodetachment, the initial state of the detached electron is described by $\ell = 2$, while the final state is a superposition of the $\ell_f = 1$ and $\ell_f = 3$ waves.^{9,10,49,50} Following the procedure similar to that outlined in Sec. III, the A_2 coefficient is defined by the following ratio (Eq. (18) with $\ell = 2$):

$$A_2 \varepsilon = \frac{\chi_{2,3}}{\chi_{2,1}} = \frac{\int_0^\infty j_3(kr)r^3 R_d(r) dr}{\int_0^\infty j_1(kr)r^3 R_d(r) dr}. \quad (33)$$

In this equation, $R_d(r)$ is the radial function of the d -like bound state, with r defined relative to the molecule’s symmetry center.

Using the origin behavior of the spherical Bessel functions (Eq. (19)) and recalling that $\varepsilon = k^2/2$, the explicit expression for A_2 that follows from Eq. (33) is shown to be

$$A_2 = \frac{2}{35} \frac{\int_0^\infty r^6 R_d(r) dr}{\int_0^\infty r^4 R_d(r) dr}. \quad (34)$$

This result is distinct from Eq. (21), as it describes photodetachment from a d rather than p orbital. Due to the r^6 and r^4 terms under the integrals in Eq. (34), the A_2 coefficient is even more sensitive to the long-range scaling of the bound orbital than the A ($\equiv A_1$) coefficient in p state detachment.

Since the d -like HOMO of O_2^- is a linear combination of $2p$ orbitals and the dominant contribution to A_2 via Eq. (34) is from the long-range part of the wavefunction, we will assume that the long-range radial dependence of the $2p\pi_g^*$ HOMO of O_2^- is determined approximately by the O $2p$ functions, i.e., $R_d(r) \approx R_{2p}(r) = \frac{1}{2\sqrt{6}} \xi_{O_2^-}^{5/2} r e^{-\xi_{O_2^-} r/2}$ (per Eq. (26)). Making this substitution in Eq. (34) yields

$$\begin{aligned} A_2 &= \frac{2}{35} \frac{\int_0^\infty r^7 e^{-\xi_{O_2^-} r/2} dr}{\int_0^\infty r^5 e^{-\xi_{O_2^-} r/2} dr} \\ &= \frac{336}{35} \frac{1}{\xi_{O_2^-}^2} \text{Hartree}^{-1} \approx (0.353/\xi_{O_2^-}^2) \text{eV}^{-1}. \end{aligned} \quad (35)$$

Parameter $\xi_{O_2^-}$ defines the spatial extent of the bound $2p\pi_g^*$ orbital in O_2^- . We will assume, initially, that $\xi_{O_2^-}$ in Eq. (35) equals ξ_{2p} in Eq. (30), as applied to O^- photodetachment. We will also adopt the notation $\xi_{2p}(O^-) \equiv \xi_{O^-}$. The physical implication of $\xi_{O_2^-} = \xi_{O^-}$ is that the long-range scaling of the parent detachment orbital does not change markedly as a result of $O^-(^2P) + O(^3P) \rightarrow O_2^-(^2\Pi_g)$ association. With this assumption, comparing Eqs. (30) and (35), the model predicts

$$A_2 = \frac{3}{5} A. \quad (36)$$

Using the experimental value of $A(O^-) = 0.55 \text{ eV}^{-1}$, we then calculate $A_2(O_2^-) = 0.33 \text{ eV}^{-1}$. Considering the crudeness of the above approximations, this prediction is in remarkable agreement with the experimentally determined range of $A_2(O_2^-) = 0.31(5) - 0.43(2) \text{ eV}^{-1}$.¹⁰

Without assuming $\xi_{O_2^-} = \xi_{O^-}$, the combination of Eqs. (30) and (35) yields

$$A_2 = \frac{3}{5} \left(\frac{\xi_{O^-}}{\xi_{O_2^-}} \right)^2 A. \quad (37)$$

As the binding energy of the $2p\pi_g^*$ electron in O_2^- (0.83 eV for vertical detachment to $v = 2$)⁵¹ is smaller than that in O^- (1.46 eV), the O_2^- wavefunction is expected to be more diffuse, described effectively by $\xi_{O_2^-} < \xi_{O^-}$. This hypothesis is confirmed by Hartree-Fock calculations using the doubly augmented basis d-aug-cc-pVQZ (chosen for its two sets of diffuse functions^{52,53}), as outlined in Supplement B of the supplementary material.³⁶ Although the Gaussian-basis description of the long-range scaling of wavefunctions has obvious limitations, the analysis suggests that the long-range tails of the individual p components of the β -spin $2p\pi_g^*$ orbital of O_2^- and $2p$ orbital of O^- are described approximately by $\xi_{O_2^-} = 1.437$ and $\xi_{O^-} = 1.511$, respectively (see Supplement B of the supplementary material).³⁶ Substituting these values in Eq. (37) and still using the experimental value of $A(O^-) = 0.55 \text{ eV}^{-1}$, we get $A_2(O_2^-) = 0.36 \text{ eV}^{-1}$, only slightly different from 0.33 eV^{-1} (obtained with $\xi_{O_2^-} = \xi_{O^-}$). Both values are well within the experimental range of $A_2 = 0.31(5) - 0.43(2) \text{ eV}^{-1}$.¹⁰

2. NH_2^- and N_3^-

We shall now use the reverse of the approach presented above (Eqs. (36) and (37)) in order to evaluate A for the a_1^{-1} photodetachment channel in NH_2^- from the A_2 coefficient determined from experimental data for N_3^- . We begin by presenting the experimental results for the azide anion.²¹ The anisotropy data in this case can be modeled in terms of detachment from a d -like anion HOMO, similar to O_2^- .

The experimental procedures are described in the Appendix and Ref. 21. The photoelectron images, spectra, and PADs for N_3^- photodetachment are shown in Figure 6.²¹ The spectra contain a single narrow band at $eBE \approx 2.66 \text{ eV}$, corresponding to the $N_3(^2\Pi_g) \leftarrow N_3(^2\Sigma_g)$ transition. The lack of an observable vibrational progression reflects the similar geometries of the anion and neutral ground states, consistent with previous studies.^{54,55} The experimentally determined anisotropy parameters are plotted vs. eKE in Figure 7.

The N_3^- HOMO is illustrated in the inset in Figure 7. While this $2p\pi_g^*$ orbital extends over the linear three-atom framework (with a node at the central nitrogen), its structure is similar to an atomic d_{xy} orbital on the central nitrogen. Fitting the $\beta(\epsilon)$ data in Figure 7 with an $\ell = 2$ WBCZ curve, yields $A_2(N_3^-) = 0.22 \text{ eV}^{-1}$. The smaller magnitude of this coefficient, relative to the $A_2 = 0.31(5) - 0.43(2) \text{ eV}^{-1}$ range for O_2^- ,¹⁰ is indicative of the smaller spatial extent of the azide orbital. Although the triatomic azide anion is geometrically larger than O_2^- , its greater detachment energy (VDE = 2.66 eV for N_3^- vs. 0.83 eV for O_2^-) corresponds to a less diffuse wavefunction and, therefore, smaller A_2 .

Since the binding energy corresponding to the N_3^- HOMO (2.66 eV) is similar to that for the a_1 (HOMO-1) in NH_2^- ($\approx 2.8 \text{ eV}$, per Figure 2(a)), we expect the spatial ex-

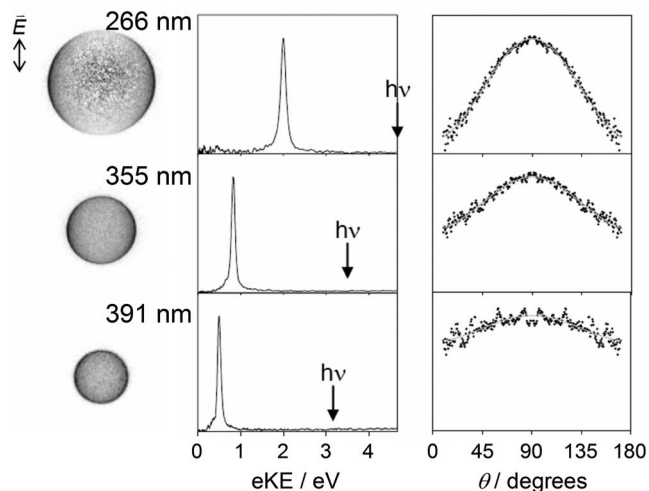


FIG. 6. Photoelectron imaging results for N_3^- at 266, 355, and 391 nm: raw photoelectron images (left; arbitrary intensity and velocity scaling), photoelectron energy spectra (middle), and photoelectron angular distributions (right). Double arrow in the top left corner indicates the laser polarization direction (vertical in the plane of all images). Vertical arrows indicate the respective photon energies. θ is photoelectron velocity angle relative to the laser polarization direction. The minimum values of all three photoelectron angular distribution axes is zero. The corresponding anisotropy parameters are plotted versus eKE in Figure 7.

tents of the two orbitals to be similar as well. Hence, we use Eq. (36) to calculate the expected value of A for the a_1^{-1} detachment transition in NH_2^- from the $A_2 = 0.22 \text{ eV}^{-1}$ determined above for N_3^- . This yields $A(NH_2^-) = 0.37 \text{ eV}^{-1}$.

This value of A applies only to the a_1^{-1} NH_2^- detachment transition, i.e., $NH_2^-(X^1A_1) \rightarrow NH_2(A^2A_1)$. The A value determined by fitting the b_1^{-1} data, i.e., $NH_2^-(X^1A_1) \rightarrow NH_2(X^2B_1)$, is significantly larger: $A = 1.09 \text{ eV}^{-1}$.¹⁹ The difference is again accounted for by the drastically different binding energies of the a_1 and b_1 orbitals, 2.8 eV and 0.8 eV, respectively (see Figure 2(a)). The smaller binding

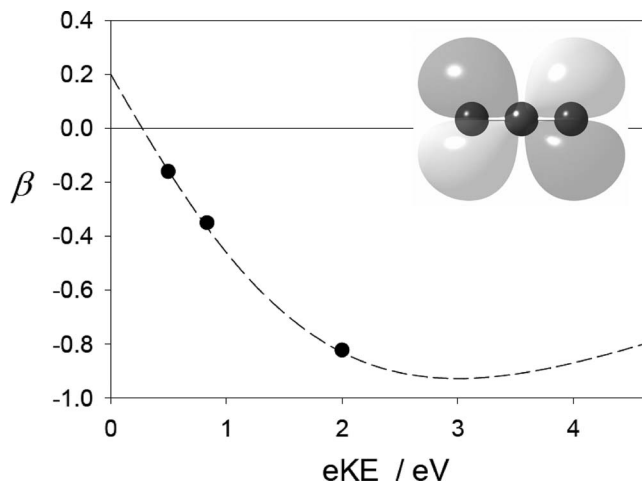


FIG. 7. Symbols: photoelectron anisotropy parameters for the $N_3(^2\Pi_g) \leftarrow N_3(^2\Sigma_g)$ photodetachment transition, determined from the data in Figure 6. The error bars are less than ± 0.1 in all cases. Dashed curve: the WBCZ (Eq. (2)) fit to the data with $\ell = 2$, $A_2 = 0.22$, and $\cos(\delta_2 - \delta_0) = 0.95$. Inset shows the π_g HOMO of N_3^- computed at the B3LYP/aug-cc-pVTZ level.

energy corresponds to a more diffuse b_1 orbital, translating into larger A .

C. Fractional p character of mixed orbitals in the central-atom approximation

We consider photodetachment from molecular orbitals localized largely on a single “central” atom. Parameter f in Eqs. (3), (6), and (7) describes the fractional p character of specific detachment orbitals, rather than the overall bonding character of the atom (related to bond angles). Despite the nominal similarities between the a_1 (HOMO-1) orbitals of CCl_2^- and NH_2^- (see Figure 1), their fractional p characters are quite different. The experimental PADs for the corresponding detachment channel in CCl_2^- (Figure 3(b)) suggest a predominantly s character of the orbital, while the data for NH_2^- (Figure 2(b)) indicate a predominantly p initial state.

Ab initio calculations support these conclusions. In this section, we quantify the fractional p characters of the CCl_2^- and NH_2^- orbitals of in the central-atom approximation, i.e., by analyzing the molecular-orbital coefficients for the s - and p -type functions of only the C and N atoms, respectively. That is, the a_1 (HOMO-1) orbitals are represented as superpositions of the $2s$ and $2p$ orbitals of C in CCl_2^- or N in NH_2^- , while the contributions of the Cl and H orbitals are ignored. For NH_2^- , we also perform an additional analysis by directly fitting a linear combination of hydrogenic $2s$ and $2p$ functions to the molecular orbital.

These analyses are carried out for Hartree-Fock MOs, neglecting electron correlation and relaxation effects. This approach is deemed sufficient within the framework of the approximate s - p mixing model. For more in-depth calculations, the use of correlated wavefunctions may be more appropriate. To this end, Oana and Krylov have demonstrated the use of Dyson orbitals in calculations of photoelectron angular distributions.^{13,14} Dyson orbitals, employed to describe photodetachment in many-electron systems, can be used in our analysis without any changes to the formalism presented in Sec. III, only at a cost of some added computational complexity.

We determined the fractional p character of the β -spin a_1 (HOMO-1) computed¹⁷ for geometry-optimized CCl_2^- by numerically integrating the radial distributions of the s and p C-atom components of the orbital (with the aug-cc-pVQZ basis set). The HF output yielded $f = 0.26$, while similar calculations at the MP2 level resulted in $f = 0.27$. The latter value will be used for CCl_2^- in the following analysis. The fractional p character of the a_1 (HOMO-1) of NH_2^- , determined in the above manner with the aug-cc-pVQZ basis set, is $f = 0.61$ at the MP2, 0.60 at the Hartree-Fock, and 0.60 at the B3LYP level. Consistent with CCl_2^- , the MP2 value of $f = 0.61$ will be used in the following analysis.

Figures 8 and 9 show (a) the computed Hartree-Fock (HOMO-1) orbitals of NH_2^- and CCl_2^- , respectively, alongside (b) the corresponding central-atom approximations, obtained using Eq. (3) with hydrogenic $2s$ and $2p$ functions and the f coefficient determined above. Clearly, the agreement between (a) and (b) is poor for both NH_2^- and CCl_2^- . In the latter case, the central-atom approximation fails significantly,

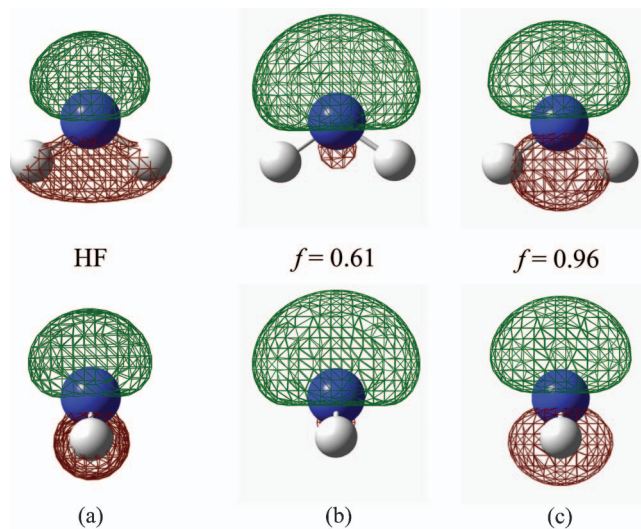


FIG. 8. (a) The a_1 (HOMO-1) orbital of NH_2^- , computed at the HF/aug-cc-pVDZ level of theory (isosurface value of 0.10). (b) The s - p mixing function defined by Eq. (3) with $f = 0.61$ from the uncorrected central-atom *ab initio* prediction. The corresponding $\beta(\epsilon)$ curve is shown in Figure 2(b) in red. (c) The least-squares fit of the model orbital defined by Eq. (3) to the computed orbital shown in (a), corresponding to $f = 0.96$. The corresponding $\beta(\epsilon)$ curve is shown in Figure 2(b) in bold black. Top and bottom in each case correspond to the same orbitals/functions viewed from two different angles.

as it cannot account for the Cl atom contributions to the MO. This problem is discussed in more detail in Sec. V B. In the case of NH_2^- , the *ab initio* orbital can in fact be adequately described as a superposition of single-center s and p functions. However, there is a significant quantitative discrepancy between the apparent p character of the MO in Figure 8(a) ($f \approx 1$) and the f value of 0.61 (Figure 8(b)) determined based on the N atom orbitals. This is because the s type functions of the H atom in NH_2^- add significantly to the overall p character of the MO.

To account approximately for the H atom contributions, we performed a least-squares fit of the model function defined by Eq. (3) to the computed (HOMO-1) of NH_2^- shown in Figure 8(a). (This is a purely *ab initio* procedure, reducing the computed wave function to a much smaller s - p mixing basis set; it does not involve a model fit to experimental data.) We procedure yields a “molecular” f value of 0.96,

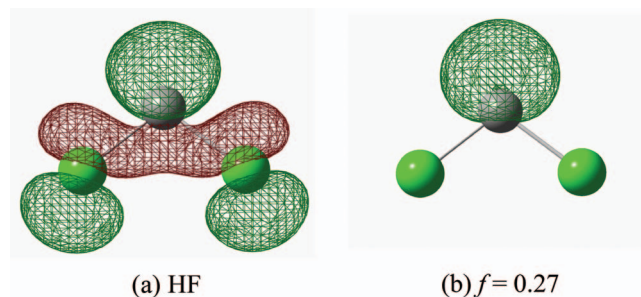


FIG. 9. (a) The a_1 (HOMO-1) orbital of CCl_2^- , computed at the HF/aug-cc-pVDZ level of theory (isosurface value of 0.04). (b) The s - p mixing model function defined by Eq. (3) with $f = 0.27$ (the uncorrected *ab initio* central-atom prediction). The corresponding $\beta(\epsilon)$ curve is shown in Figure 3(b) in red.

corresponding to $\sqrt{1-f} = 0.20$ for the s coefficient in Eq. (3). The corresponding s - p model function is plotted in Figure 8(c), reflecting a much improved agreement with the *ab initio* MO, compared to the orbital in Figure 8(b).

Similar analysis for the CCl_2^- HOMO-1 (depicted in Figure 9(a)) is not meaningful, because the contributions of Cl p functions to the MO cannot be accounted for, even approximately, within the central-atom s - p mixing model.

V. COMPARISON TO EXPERIMENT

A. Application of the s - p mixing model to NH_2^- and CCl_2^-

We now compare the model predictions using the parameter values determined in Sec. IV, to the experimental data for NH_2^- and CCl_2^- introduced in Sec. II. The model predictions (not fits to the data) for the a_1^{-1} photodetachment channels in these anions are shown by solid curves in Figures 2(b) and 3(b), respectively. All NH_2^- calculations assume $A = 0.37 \text{ eV}^{-1}$, while the CCl_2^- curves use $A = 0.75 \text{ eV}^{-1}$. Justification for these values is given in Secs. IVA and IV B.

Several model curves are included in each of Figures 2(b) and 3(b). First, the WBCZ model predictions for pure p state photodetachment are shown for reference (green), calculated using Eq. (6) with $f = 1$ or, equivalently, Eq. (2) with $\ell = 1$. In addition, Figure 3(b) includes a horizontal $\beta = 2$ line (also green) for the pure s state limit (Eq. (6) with $f = 0$ or, equivalently, Eq. (2) with $\ell = 0$).

Next, two mixed s - p curves are shown in each case. For NH_2^- , the red curve in Figure 2(b) was calculated assuming the unmodified parameters $B/A = 8/3$ (Eq. (32)) and $f = 0.61$, i.e., $Z = (B/A)(1-f)/f = 1.7$. The $f = 0.61$ value corresponds to the central-atom approximation accounting for N contributions only (Sec. IV C). The bold black curve in Figure 2(b) corresponds to $f = 0.96$ ($Z = 0.11$), which corrects for the H atoms contributions to the MO, as also discussed in Sec. IV C. Although this last simulation is still rooted in the central-atom formalism, the above simple correction yields a much better quantitative agreement with the experiment.

For the a_1 (HOMO-1) of CCl_2^- , the central-atom approximation is not justified (Sec. IV C). However, assuming that the photodetachment occurs predominantly from the carbene center in the anion, the s - p mixing model can provide an approximate description of the experimental observations in terms of adjustable parameter Z . The red curve in Figure 3(b) assumes the unmodified *ab initio* parameters values: $B/A = 8/3$ (Eq. (32)) and $f = 0.27$ (Sec. IV C), i.e., $Z = (B/A)(1-f)/f = 7.2$. Despite the quantitative discrepancies, this simulation (not fit to the data) does capture the qualitative trend in the data.

The black curve in Figure 3(b) is calculated assuming a Z value adjusted for best agreement of the model with the experiment. The curve is shown as dashed, because it represents the only simulation in this work that involves a fit to experimental data, in addition to *ab initio* modeling. The dashed curve corresponds to $Z = 27$, which can be obtained, for example, with $B/A = 8/3$ (Eq. (32)) and $f = 0.09$. Thus, the experimental re-

sults (fit with the dashed black curve) fall closer to the pure s state limit (larger Z) than the unmodified model prediction (red solid curve). The direction of this deviation reflects certain qualitative features of the electronic structure of CCl_2^- , discussed in Sec. V B.

B. Breakdown of the central-atom approximation

Some discrepancies between the approximate model and the experiment are to be expected. Yet, in the case of NH_2^- the black curve in Figure 2(b), calculated entirely based on *ab initio* values, provides a nearly quantitative agreement with the experiment. The remaining divergence may likely be accounted for by the neglected phase shifts. In the CCl_2^- case, the quantitative divergence of the model from the experiment is attributed to the breakdown of the central-atom approximation. Although quantitative modeling outside of this approximation is beyond the scope of this work, we present arguments that explain the direction of the observed discrepancy.

With a given value of A , the anisotropy trends described by Eq. (7) are uniquely determined by $Z \equiv (B/A)(1-f)/f$. As f by itself is not a meaningful parameter for CCl_2^- , because of the breakdown of the central-atom approximation, we use Z to describe the model curves in Figure 3(b). While *ab initio* (central-atom) modeling yields $Z = 7.2$ (red curve in Figure 3(b)), the experimental data suggest $Z \approx 27$ (dashed black curve). The difference can be understood in two ways. (i) If the B/A ratio is kept fixed at the unmodified model value of $8/3$, the larger experimental Z value reflects a smaller fractional p character of the parent orbital: $f \approx 0.09$, compared to the central-atom estimate of $f = 0.27$. (ii) If, on the other hand, $f = 0.27$ is kept unchanged, the experimental value of Z corresponds to $B/A \approx 10$, a marked increase from the model prediction of $B/A = 8/3$.

The above parameter adjustments may be explained by the properties of the parent orbital, shown in Figure 9(a). The analysis of the dominant s and p contributions of all atoms, not just C, indicates that the Cl s function contributions to the MO are small, but contributions from the Cl p functions are non-negligible. The respective p contributions of Cl and C are opposite in sign and the resulting interference can be accounted for, approximately, by adjusting either the (i) f or (ii) B/A model parameters, which results in an overall increase in Z .

- (i) The destructive overlap of the C and Cl p functions in the short range effectively reduces the p character of the orbital. Assuming unmodified $B/A = 8/3$, these considerations are consistent with the increased value of Z that best describes the data in Figure 3(b).
- (ii) The destructive interference of the C and Cl p functions in the long range can be accounted for, approximately, within the central-atom approximation by increasing ξ_{2p} relative to ξ_{2s} and turning to Eq. (31), which reflects the variation of B/A with respect to ξ_{2s} and ξ_{2p} . As there is no significant s contribution from the Cl atoms to the MO of interest, the s part of the orbital remains well represented by the central-atom approximation and there is no reason to modify ξ_{2s} . Thus, we expect $\xi_{2p}/\xi_{2s} > 1$, suggesting that $B/A \gg 8/3$ (the “much greater than”

sign is due to the 7th power in Eq. (31)), which is consistent with the $B/A \approx 10$ value that the experimental data in Figure 3(b) suggest (assuming unmodified $f = 0.27$).

Thus, considering the basic features of the electronic structure indicates how adjustments to the parameters can help overcome the breakdown of the central-atom approximation.

C. Polarization-induced $n's$ - np mixing ($n' \neq n$)

Finally, we comment on the $n's$ - np ($n' \neq n$) mixing that may be used to describe a variety of solvated anion systems. This approach was adopted in our previous work on $H^-(NH_3)_n$ and $NH_2^-(NH_3)_n$ cluster anions.^{15,19} We revisit this type of initial states on the example of $H^-(NH_3)_n$ in order to illuminate one pertinent aspect of anion solvation in the light of the present work.

In Sec. III E, we showed that for the $1s$ - $2p$ mixing scenario, applicable to solvated H^- , $B/A = (1/768)(\xi_{2p}/\xi_{1s})$,⁷ with $\xi_{1s} > \xi_{2p}$ mandated by the very diffuse nature of the solvation-induced polarization component. Calculating the appropriate values of ξ_{1s} and ξ_{2p} is beyond the scope of the present work, but because of the high power dependence on ξ_{2p}/ξ_{1s} , a B/A ratio $< 10^{-3}$ can easily be expected. The original analysis of $H^-(NH_3)_n$ anisotropies yielded a reasonable agreement with the experiment using $f \approx 0.03$ and arbitrarily assuming $B = A$ (i.e., $B/A = 1$), as the properties of the B/A ratio had not been known at the time.¹⁵ Since it is $Z \equiv (B/A)(1 - f)/f$, rather than B/A and f separately, that determines the anisotropy trends (Eq. (7)), the above values of f and B/A should be interpreted in terms of the single parameter $Z \approx 30$. If $B/A < 10^{-3}$, then with no substantive changes in the original analysis,¹⁵ we deduce that a polarization-induced fractional p character $f < 3 \times 10^{-5}$ is indicated by the experimental results for solvated H^- .

VI. SUMMARY

We have presented an approximate model for photoelectron angular distributions in anion photodetachment from mixed s - p states. Considering the resulting dipole-allowed s , p , and d free-electron partial waves allows us to make predictions for the photoelectron anisotropy in terms of the fractional p character of the detachment orbital and the A and B coefficients describing the relative intensities of the $p \rightarrow d$ to $p \rightarrow s$ and $s \rightarrow p$ to $p \rightarrow s$ channels, respectively.

The primary objective of the model is to provide conceptual insight into the physics of photodetachment from hybrid or mixed molecular orbitals, without embarking on computerized calculations. It was developed assuming the following approximations: (i) The only contributions to the parent orbital that were considered are those from the s and p components of the central atom. The breakdown of this approximation was also discussed. (ii) Analytical solutions of the model have been obtained within the low-eKE approximation, the same approximation that allows rewriting the Cooper-Zare equation (Eq. (1)) in the WBCZ form (Eq. (2)). (iii) Further analytical solutions have been obtained assuming that the

long-range tails of anionic wavefunctions can be described in terms of hydrogenic wavefunctions, with the effective nuclear charge parameter used to control the spatial extent of the tails.

For the case of hydrogenic orbitals, it has been shown that the B/A ratio in photodetachment from a mixed $2s$ - $2p$ state equals $8/3$ (assuming the same spatial extents of the s and p tails). Corresponding fractions have also been derived for other ns - np mixing cases.

The predictions of the model were tested using several model anion systems, including NH_2^- and CCl_2^- . The agreement with the experiment is quite compelling for NH_2^- , while the quantitative discrepancies in the CCl_2^- case are attributed to the breakdown of the central-atom approximation. A mechanism for corresponding corrections has been indicated.

ACKNOWLEDGMENTS

This work was supported by the U.S. National Science Foundation (Grant No. CHE-1011895). A.S. acknowledges additional support from the Dr. Emily Davis and Dr. Homer C. Weed Endowment. L.M.C. thanks the State of Arizona TRIF Imaging Fellowship program. We would like to thank Dr. Ian Jones for assistance in the synthesis of benzyl azide, a precursor for the N_3^- anions. Stimulating discussions with Dr. Laura O. Van Dorn are gratefully acknowledged.

APPENDIX: EXPERIMENTAL DETAILS

The experiments were performed using the pulsed negative-ion photoelectron imaging spectrometers described in detail elsewhere.^{4,16,56} In each case, a neutral precursor gas is expanded through a pulsed supersonic nozzle (General Valve, Inc., series 9) operated at a 50 Hz repetition rate into a vacuum chamber ($\sim 10^{-6}$ Torr base pressure, $\sim 10^{-5}$ Torr under load), where it is bombarded with a crossed or counter-propagating continuous beam of 1 keV electrons from an electron gun. Negative ions⁵⁷ from the resulting plasma are extracted into a Wiley-McLaren⁵⁸ time-of-flight mass-spectrometer by a pulsed repeller plate downstream of the nozzle.⁵⁹ The resulting mass-spectra are recorded using a dual microchannel plate detector positioned at the end of a ~ 2 m long flight tube.

Photoelectron images are obtained by intersecting a linearly polarized laser pulse with the ion packet of interest about 15 cm upstream of the ion detector, within a velocity-map⁶⁰ imaging⁶¹ assembly ($\sim 10^{-8}$ Torr operating pressure). Photodetachment is performed using the harmonics of a nanosecond pulsed Nd:YAG laser operating at a repetition rate of 50 kHz (Quanta Ray Lab 130-50 by Spectra Physics, Inc.) or the fundamental or the second or third harmonics of an amplified femtosecond Ti:Sapphire laser (Spectra Physics, Inc.).

The photoelectron images are collected over 10^4 - 10^5 experimental cycles each. The photodetached electrons are accelerated by a series of electrodes onto a 40 mm diameter microchannel plate detector, coupled to a P43 phosphor screen (Burle, Inc.). The resulting images are recorded by a charge-coupled device camera. Typically, 10^4 - 10^5 experimental cycles are accumulated for each reported image. The photodetachment transitions for bare H^- (Ref. 62) and O^-

(Ref. 63 and 64) are used for energy calibration. The complete three-dimensional photoelectron distributions are reconstructed using the inverse Abel transform,⁶⁵ as implemented in the BASEX program.⁶⁶

The CCl_2^- anions were synthesized via a gas-phase ion-molecule reaction within the supersonic expansion of dichloromethane seeded in N_2O carrier gas at a backing pressure of ~ 30 psi.^{20,67,68} High-energy electron collisions produced slow secondary electrons, which formed O^- by dissociative electron attachment to N_2O , followed by the desired H_2^+ abstraction reaction of O^- with CH_2Cl_2 , giving CCl_2^- .

For NH_2^- generation, a neutral precursor of neat ammonia or 30% ammonia seeded in argon was used. The resulting mass-spectra contained two series of peaks, corresponding to the $\text{H}^-(\text{NH}_3)_n$ and $\text{NH}_2^-(\text{NH}_3)_n$ cluster-ion series, exclusively.¹⁹

Azide ions, N_3^- , were generated by dissociative electron attachment to benzyl azide,^{54,69} which was prepared as follows based upon a common synthesis,⁷⁰ as described in Ref. 21. (Though no problems were encountered during this synthesis, some azides are known to be explosive. A careful analysis of safety hazards should be performed before attempting to recreate this synthesis. Details in Ref. 21) Benzyl azide was seeded in argon by passing the argon carrier gas with a stagnation pressure of ~ 25 psig through a stainless steel sample holder containing ~ 100 mg of benzyl azide approximately 6 in. upstream of the nozzle. Azide formation is expected to occur via dissociative secondary electron attachment to benzyl azide.^{54,69} Azide was identified in the time-of-flight mass-spectrum and photodetached with the second harmonic from a Ti:Sapphire laser (391 nm) and the third (355 nm) and fourth (266 nm) harmonics of a Nd:YAG laser.

- ¹J. Cooper and R. N. Zare, in *Atomic Collision Processes*, edited by S. Geltman, K. T. Mahanthappa, and W. E. Brittin (Gordon and Breach, New York/London/Paris, 1968), Vol. XI-C, p. 317.
- ²T. Seideman, *J. Chem. Phys.* **113**, 1677 (2000).
- ³K. L. Reid, *Annu. Rev. Phys. Chem.* **54**, 397 (2003).
- ⁴A. Sanov and R. Mabbs, *Int. Rev. Phys. Chem.* **27**, 53 (2008).
- ⁵H. A. S. Bethe and E. E. Salpeter, *Quantum Mechanics of One- and Two-Electron Atoms* (Springer-Verlag/Academic, Berlin/New York, 1957).
- ⁶J. Cooper and R. N. Zare, *J. Chem. Phys.* **48**, 942 (1968).
- ⁷J. Cooper and R. N. Zare, *J. Chem. Phys.* **49**, 4252 (1968).
- ⁸K. J. Reed, A. H. Zimmerman, H. C. Andersen, and J. I. Brauman, *J. Chem. Phys.* **64**, 1368 (1976).
- ⁹F. A. Akin, L. K. Schirra, and A. Sanov, *J. Phys. Chem. A* **110**, 8031 (2006).
- ¹⁰M. Van Duzor, F. Mbaïwa, J. Wei, T. Singh, R. Mabbs, A. Sanov, S. J. Cavanagh, S. T. Gibson, B. R. Lewis, and J. R. Gascooke, *J. Chem. Phys.* **133**, 174311 (2010).
- ¹¹J. G. Underwood and K. L. Reid, *J. Chem. Phys.* **113**, 1067 (2000).
- ¹²T. Seideman, *Annu. Rev. Phys. Chem.* **53**, 41 (2002).
- ¹³C. M. Oana and A. I. Krylov, *J. Chem. Phys.* **127**, 234106 (2007).
- ¹⁴C. M. Oana and A. I. Krylov, *J. Chem. Phys.* **131**, 124114 (2009).
- ¹⁵E. Grumblin and A. Sanov, *J. Chem. Phys.* **135**, 164302 (2011).
- ¹⁶E. Surber, R. Mabbs, and A. Sanov, *J. Phys. Chem. A* **107**, 8215 (2003).
- ¹⁷M. J. Frisch, G. W. Trucks, H. B. Schlegel *et al.*, GAUSSIAN 98, Gaussian, Inc., Pittsburgh, PA, 1998.
- ¹⁸S. W. Wren, K. M. Vogelhuber, K. M. Ervin, and W. C. Lineberger, *Phys. Chem. Chem. Phys.* **11**, 4745 (2009).
- ¹⁹E. Grumblin and A. Sanov, *J. Chem. Phys.* **135**, 164301 (2011).
- ²⁰D. J. Goebbert, K. Pichugin, D. Khuseynov, P. G. Wenthold, and A. Sanov, *J. Chem. Phys.* **132**, 224301 (2010).
- ²¹E. R. Grumblin, Ph.D. dissertation, University of Arizona, 2010.
- ²²R. J. Celotta, R. A. Bennett, and J. L. Hall, *J. Chem. Phys.* **60**, 1740 (1974).
- ²³S. Roszak, *J. Chem. Phys.* **105**, 7569 (1996).

- ²⁴J. T. Snodgrass, J. V. Coe, C. B. Freidhoff, K. M. McHugh, S. T. Arnold, and K. H. Bowen, *J. Phys. Chem.* **99**, 9675 (1995).
- ²⁵K. K. Murray, D. G. Leopold, T. M. Miller, and W. C. Lineberger, *J. Chem. Phys.* **89**, 5442 (1988).
- ²⁶D. Hanstorp, C. Bengtsson, and D. J. Larson, *Phys. Rev. A* **40**, 670 (1989).
- ²⁷S. J. Cavanagh, S. T. Gibson, M. N. Gale, C. J. Dedman, E. H. Roberts, and B. R. Lewis, *Phys. Rev. A* **76**, 052708 (2007).
- ²⁸E. R. Grumblin, K. Pichugin, L. Velarde, and A. Sanov, *J. Phys. Chem. A* **114**, 1367 (2010).
- ²⁹A. V. Davis, R. Wester, A. E. Bragg, and D. M. Neumark, *J. Chem. Phys.* **118**, 999 (2003).
- ³⁰M. K. Gilles, K. M. Ervin, J. Ho, and W. C. Lineberger, *J. Phys. Chem.* **96**, 1130 (1992).
- ³¹R. Mabbs, E. Surber, and A. Sanov, *J. Chem. Phys.* **122**, 054308 (2005).
- ³²E. P. Wigner, *Phys. Rev.* **73**, 1002 (1948).
- ³³J. V. Ortiz, *Int. J. Quantum Chem.* **100**, 1131 (2004).
- ³⁴L. D. Landau and E. M. Lifshitz, *Quantum Mechanics: Nonrelativistic Theory*, 3rd ed. (Pergamon, Oxford, 1977).
- ³⁵C. Cohen-Tannoudji, B. Diu, and F. Laloë, *Quantum Mechanics* (Wiley, New York/London/Sydney/Toronto, 1977).
- ³⁶See supplementary material at <http://dx.doi.org/10.1063/1.4789811> for discussion of (A) free-electron wave normalization; (B) the role of very diffuse anionic wavefunctions; (C) the validity of the low-eKE approximation; (D) analytically evaluated integrals appearing in Eqs. (21), (23), and (24).
- ³⁷L. C. Green, S. Matsuchima, and E. K. Kolchin, *Astrophys. J., Suppl. Ser.* **3**, 459 (1958).
- ³⁸H. A. Bethe, *Handbuch der Physik* **24**, 483 (1933).
- ³⁹S. M. Goldberg, C. S. Fadley, and S. Kono, *J. Electron Spectrosc. Relat. Phenom.* **21**, 285 (1981).
- ⁴⁰W. C. Lineberger, H. Hotop, and T. A. Patterson, in *Electron and Photon Interactions with Atoms*, edited by H. Kleinpoppen and M. R. C. McDowell (Plenum, New York, 1976), p. 125.
- ⁴¹R. D. Mead, K. R. Lykke, and W. C. Lineberger, in *Electronic and Atomic Collisions*, edited by J. Eichler, I. V. Hertel, and N. Stolterfoht (Elsevier, 1984), p. 721.
- ⁴²J. L. Hall and M. W. Siegel, *J. Chem. Phys.* **48**, 943 (1968).
- ⁴³W. D. Brandon, D. H. Lee, D. Hanstorp, and D. J. Pegg, *J. Phys. B* **31**, 751 (1998).
- ⁴⁴F. Breyer, P. Frey, and H. Hotop, *Z. Phys. A: Hadrons Nucl.* **286**, 133 (1978).
- ⁴⁵J. C. Slater, *Phys. Rev.* **36**, 57 (1930).
- ⁴⁶E. Clementi and D. L. Raimondi, *J. Chem. Phys.* **38**, 2686 (1963).
- ⁴⁷M. Scheer, R. C. Bilodeau, C. A. Brodie, and H. K. Haugen, *Phys. Rev. A* **58**, 2844 (1998).
- ⁴⁸D. J. Pegg, C. Y. Tang, J. Dellwo, and G. D. Alton, *J. Phys. B* **26**, L789 (1993).
- ⁴⁹R. J. Celotta, R. A. Bennett, J. Levine, J. L. Hall, and M. W. Siegel, *Phys. Rev. A* **6**, 631 (1972).
- ⁵⁰R. Mabbs, F. Mbaïwa, J. Wei, M. Van Duzor, S. T. Gibson, S. J. Cavanagh, and B. R. Lewis, *Phys. Rev. A* **82**, 011401 (2010).
- ⁵¹K. M. Ervin, W. Anusiewicz, P. Skurski, J. Simons, and W. C. Lineberger, *J. Phys. Chem. A* **107**, 8521 (2003).
- ⁵²R. A. Kendall, T. H. Dunning, and R. J. Harrison, *J. Chem. Phys.* **96**, 6796 (1992).
- ⁵³D. E. Woon and T. H. Dunning, *J. Chem. Phys.* **100**, 2975 (1994).
- ⁵⁴R. E. Continetti, D. R. Cyr, R. B. Metz, and D. M. Neumark, *Chem. Phys. Lett.* **182**, 406 (1991).
- ⁵⁵X. Yang, B. Kiran, X. B. Wang, L. S. Wang, M. Mucha, and P. Jungwirth, *J. Phys. Chem. A* **108**, 7820 (2004).
- ⁵⁶L. Velarde, T. Habteyes, and A. Sanov, *J. Chem. Phys.* **125**, 114303 (2006).
- ⁵⁷M. A. Johnson and W. C. Lineberger, in *Techniques for the Study of Ion Molecule Reactions*, edited by J. M. Farrar and W. H. Saunders (Wiley, New York, 1988), p. 591.
- ⁵⁸W. C. Wiley and I. H. McLaren, *Rev. Sci. Instrum.* **26**, 1150 (1955).
- ⁵⁹E. Surber, S. P. Ananthavel, and A. Sanov, *J. Chem. Phys.* **116**, 1920 (2002).
- ⁶⁰A. T. J. B. Eppink and D. H. Parker, *Rev. Sci. Instrum.* **68**, 3477 (1997).
- ⁶¹D. W. Chandler and P. L. Houston, *J. Chem. Phys.* **87**, 1445 (1987).
- ⁶²K. R. Lykke, K. K. Murray, and W. C. Lineberger, *Phys. Rev. A* **43**, 6104 (1991).
- ⁶³C. Valli, C. Blondel, and C. Delsart, *Phys. Rev. A* **59**, 3809 (1999).
- ⁶⁴D. M. Neumark, K. R. Lykke, T. Andersen, and W. C. Lineberger, *Phys. Rev. A* **32**, 1890 (1985).

- ⁶⁵A. J. R. Heck and D. W. Chandler, *Annu. Rev. Phys. Chem.* **46**, 335 (1995).
- ⁶⁶V. Dribinski, A. Ossadtchi, V. A. Mandelshtam, and H. Reisler, *Rev. Sci. Instrum.* **73**, 2634 (2002).
- ⁶⁷D. J. Goebbert, D. Khuseynov, and A. Sanov, *J. Phys. Chem. A* **114**, 2259 (2010).
- ⁶⁸D. J. Goebbert, D. Khuseynov, and A. Sanov, *J. Phys. Chem. A* **115**, 3208 (2011).
- ⁶⁹E. Illenberger, P. B. Comita, J. I. Brauman, H. P. Fenzlaff, M. Heni, N. Heinrich, W. Koch, and G. Frenking, *Ber. Bunsenges. Phys. Chem.* **89**, 1026 (1985).
- ⁷⁰S. G. Alvarez and M. T. Alvarez, *Synthesis-Stuttgart* **4**, 413 (1997).